INTERNATIONAL JOURNAL FOR NUMERICAL METHODS IN FLUIDS
Int. J. Numer. Meth. Fluids 2003; **43**:1107–1137 (DOI: 10.1002/fld.529)

Numerical solutions of incompressible Navier–Stokes equations using modified Bernoulli's law

A. Shatalov*,† and M. Hafez

Department of Mechanical and Aeronautical Engineering, University of California, Davis, CA 95616, U.S.A.

SUMMARY

Simulations of incompressible flows are important for many practical applications in aeronautics and beyond, particularly in the high Reynolds number regime. The present formulation is based on Helmholtz velocity decomposition where the velocity is presented as the gradient of a potential plus a rotational component. Substituting in the continuity equation yields a Poisson equation for the potential which is solved with a zero normal derivative at solid surfaces. The momentum equation is used to update the rotational component with no slip/no penetration surface boundary conditions. The pressure is related to the potential function through a special relation which is a generalization of Bernoulli's law, with a viscous term included. Results of calculations for two- and three-dimensional problems prove that the present formulation is a valid approach, with some possible benefits compared to existing methods. Copyright © 2003 John Wiley & Sons, Ltd.

KEY WORDS: incompressible flows; Navier–Stokes equations; modified Bernoulli's law; viscous-inviscid interaction

1. INTRODUCTION

Numerical simulation of incompressible flows is a useful tool to study many interesting problems of fluid mechanics, beyond aeronautics, for example flow around cars and buildings, flow in rivers and channels, blood flow and many others.

Gases at low speeds, behave like liquids, namely, density can be considered constant in the absence of heat, so there are applications including the motion of air and the motion of water based on the same incompressible flow models.

Numerical simulations of incompressible flows are well developed (see References [1–7]). There are many algorithms available nowadays to solve Navier–Stokes equations, in many forms and there are many commercial codes, based on these algorithms, and are used to solve practical problems. Nevertheless, the research in this field has not stopped, as indicated by this work for at least two reasons. First, there are open questions regarding some of the existing methods. Second, there is always a need for improvement and with computers getting cheaper and more powerful, in both speed and memory, it is worthwhile to consider new ideas.

* Correspondence to: A. Shatalov, Department of Mechanical and Aeronautical Engineering, University of California, Davis, CA 95616, U.S.A.
† E-mail: mhafez@ucdavis.edu

Received 1 April 2002
Revised 15 January 2003

Copyright © 2003 John Wiley & Sons, Ltd.

For two-dimensional (and axisymmetric) flows, the stream function/vorticity formulation of Navier–Stokes equations have been used since the 1940s. In the 1960s, three algorithms were introduced to solve the primitive variable forms of Navier–Stokes equations. Harlow and Welch [8] solved a Poisson equation, obtained from the divergence of the momentum equation, to calculate the pressure. Chorin [9] introduced the artificial compressibility method by adding an artificial time derivative term of the pressure to the continuity equation, with a coefficient related to the associated artificial speed of sound. Steady-state solutions are obtained for the modified initial/boundary value problems; dual time steps were introduced later by Kwak *et al.* [10] as well as by Merkle [11] for calculations of time-dependent problems. Chorin [12] introduced also the projection method where he decomposed the velocity into two parts; the correction to the velocity obtained from the momentum equation is assumed to be proportional to the gradient of the pressure. Substituting such a decomposition into the continuity equation yields again a Poisson equation for the pressure (the slip velocity, however, may not be exactly enforced at the discrete level; so, it is not zero to machine accuracy). Other related methods are the vector potential and velocity/vorticity formulations. See Reference [13] for more details.

Finite differences and finite volumes on staggered and regular (collocated) grids have been used in many applications (see References [14–16]). Finite-element formulations, on the other hand, are usually based on different interpolations for the velocity and for the pressure. The same interpolation can be used, if artificial viscosity is added to the continuity equation. In this case, discrete mass is not conserved to machine accuracy [17, 18]. In all cases, iterative methods are used to solve the non-linear algebraic equations resulting from the discretization process.

In the present work, a velocity decomposition is used where the velocity is represented as a gradient of a potential plus a rotational component. The potential is related to the pressure in a special form which is a generalization of Bernoulli's law, including a viscous term, i.e. a modified Bernoulli's law.

In the following, the details of the formulation will be discussed and some simple problems, where for convenience only Cartesian grids are required, will be solved. Standard numerical methods will be employed. All terms are approximated using central differences except for the convective terms, where upwinding is introduced. The discrete equations are solved iteratively via line relaxations, in a segregated manner.

The examples are chosen to demonstrate viscous/inviscid interaction for internal and external flows in two and three dimensions. Incompressible two-dimensional flows over infinite and finite flat plate, flows with pressure gradient and with suction as well as flows over obstacles are studied. For three dimensions, flows over a finite plate, corner flows and flows in ducts with square cross-sections are simulated to confirm the validity of the present formulation. Finally, possible merits and further studies are discussed in the conclusion section.

2. PRESENT FORMULATION, GOVERNING EQUATIONS, AND BOUNDARY CONDITIONS

2.1. Motivation

Consider high-Reynolds-number flows over streamlined bodies. The viscous stresses are confined to boundary layers and wakes. Outside these thin layers, the flow is inviscid and

Copyright © 2003 John Wiley & Sons, Ltd.

irrotational for uniform upstream conditions. In the viscous/inviscid interaction procedures, boundary-layer equations are solved to provide the displacement thickness distributions. The potential flow equation is solved over the original bodies augmented with the displacement thickness, where the velocity is calculated as the gradient of the potential and the pressure is obtained via Bernoulli's law. Iterations are required to solve the boundary-layer equations with the pressure gradient obtained from the potential flow calculations. Convergence of such iterative procedures usually suffers, particularly in the case of separated flows. Although, in principle, boundary-layer approximations are not valid for separated flows, specially at separation and reattachment points, interactive boundary-layer calculations produce acceptable results, at least for engineering applications, provided the convergence of the interactive procedure is not a problem. Boundary-layer approximations are not, however, valid in other regions, for example at the trailing edges, and more important at corners and wing tips.

In the same spirit of interactive boundary-layer calculations, zonal approaches were introduced, where the potential flow equation is solved in the outer region while Navier–Stokes equations are solved in the inner region. An artificial, internal boundary between the two regions must be handled correctly, otherwise errors will be reflected from these boundaries during iterations and convergence becomes slow [19]. Accuracy of the calculations can be also affected. Usually, there is an overlap region and a Schwartz-type iteration can be developed. Thus, the potential flow provides boundary condition for Navier–Stokes calculations which is limited to the viscous flow region. In return, there is a feedback in terms of the mass flux as boundary conditions for the potential flow.

In the present formulation, some of these ideas are combined in a new and different way to have their advantages without the associated penalties. Let us consider, just for the sake of demonstration, the stream function/vorticity formulation for two-dimensional problems. Navier–Stokes equations can be written in the form

$$\psi_{xx} + \psi_{yy} = -\omega \tag{1}$$

$$u\omega_x + v\omega_y = \frac{1}{Re}(\omega_{xx} + \omega_{yy}) \tag{2}$$

with the boundary conditions at the solid surface

$$\psi = \text{constant} \tag{3}$$

$$\frac{\partial \psi}{\partial n} = 0 \tag{4}$$

where **n** is the normal to the solid boundary. Equation (3) imposes the no surface penetration condition while Equation (4) is the no-slip condition. In the far field, a uniform flow, with no vorticity, is imposed on the calculation, except downstream of the wake where boundary layer approximation can be used as a non-reflecting boundary condition, namely,

$$\psi_{yy} = -\omega \tag{5}$$

$$u\omega_x + v\omega_y = \frac{1}{Re}\omega_{yy} \tag{6}$$

Copyright © 2003 John Wiley & Sons, Ltd.

Notice, backward difference approximation for ω_x will eliminate any need for downstream information. Since the vorticity vanishes outside the viscous layer, Equation (2) is solved only in the viscous region. One can set $\omega = 0$ in the outer region (the viscous region can be *a priori* estimated conservatively for many problems). The distributed vorticity, generated in the viscous region, plays the role of a forcing function (non-homogeneous term) in the stream-function equation. The latter is solved everywhere in the field and reduces automatically to the irrotational flow equation in the outer region. To have an acceptable resolution of the physics, a fine mesh must be used in the viscous region, with a characteristic length comparable to the boundary-layer thickness, while a coarser mesh can be used in the inviscid flow where the characteristic length is the body length. Such a strategy has been tested in Reference [20] and it was shown that it is more efficient than the alternating Schwartz iteration.

Unfortunately, it is not easy to extend the above formulation to three-dimensional problems. At least, two stream functions and two vorticity components are needed and the boundary conditions at the solid surface become complicated. In References [21, 22] Cauchy/Riemann equations for the velocity components are used to overcome these difficulties. However, the three velocity components must be calculated everywhere in the viscous and in the inviscid regions.

In the present work, the potential function is used instead, using Helmholtz velocity decomposition. The rotational components are calculated only in the viscous region. In some sense, this approach is an attempt to develop an equivalent system of the stream function/vorticity formulation but it is not restricted to two dimensions.

2.2. *Helmholtz velocity decomposition*

According to a main theorem of vector analysis due to Helmholtz, a vector can be decomposed into a curl free component and a divergence free component, under very general conditions (e.g. the vector magnitude must be bounded in the far field).

In the present work, we use the following velocity decomposition:

$$\mathbf{q} = \nabla\phi + \mathbf{q}^* \tag{7}$$

where ϕ is a potential function and $\mathbf{q}^*$ is the rotational component of the velocity field. Since the curl of the gradient vanishes ($\nabla \times \nabla\phi = 0$), Equation (7) leads to

$$\nabla \times \mathbf{q} = \nabla \times \mathbf{q}^* \tag{8}$$

Similar decompositions have been used in the literature for flow simulations in many ways. See for example, the recent work of Nikfetrat and Hafez [23, 24] for a review and in particular, see References [15, 25–33].

The main feature in the present work is that ϕ is related to the pressure in a specified form as will be shown below.

Substituting Equation (7) in the continuity equation yields

$$\nabla^2\phi = -\nabla \cdot \mathbf{q}^* \tag{9}$$

Equation (9) is a Poisson equation for the potential function ϕ, where the forcing function (non-homogeneous term) is related to the divergence of the rotational component of the velocity.

Copyright © 2003 John Wiley & Sons, Ltd.

Alternately, substituting Equation (7) in the normalized momentum equation yields

$$(\mathbf{q}\cdot\nabla)\mathbf{q}^* = g + \frac{1}{Re}\nabla^2\mathbf{q}^* \tag{10}$$

where $g = g_1 + g_2$, and

$$g_1 = -\nabla\left(P + \frac{1}{2}(\nabla\phi)^2 - \frac{1}{Re}(\nabla^2\phi)\right)$$

$$g_2 = -(\mathbf{q}^*\cdot\nabla)\nabla\phi$$

In the above equation, P is the static pressure, and g_1 is set equal to zero. The rational behind this choice is that the vorticity in terms of $\mathbf{q}^*$ (i.e. $\nabla\times\mathbf{q}^*$) should be independent of g_1 since the latter is a gradient of a scalar function. Hence, $\mathbf{q}^*$ is obtained from

$$(\mathbf{q}\cdot\nabla)\mathbf{q}^* = -(\mathbf{q}^*\cdot\nabla)\nabla\phi + \frac{1}{Re}\nabla^2\mathbf{q}^* \tag{11}$$

The pressure is obtained from the modified Bernoulli's law:

$$P + \frac{1}{2}(\nabla\phi)^2 - \frac{1}{Re}(\nabla^2\phi) = \text{constant} \tag{12}$$

Notice, the pressure is not needed during the iteration. After convergence, the pressure is given in terms of ϕ as indicated by Equation (12). The constant on the right side is evaluated in terms of upstream uniform conditions.

2.3. Boundary conditions

The choice of boundary conditions for the potential function ϕ is important in this formulation to satisfy the requirement that the potential function represents the inviscid flow region. Therefore, at a solid surface

$$\frac{\partial\phi}{\partial n} = 0 \tag{13}$$

Hence, from the no penetration boundary condition

$$\mathbf{q}^*\cdot\mathbf{n} = 0 \tag{14}$$

The no-slip boundary condition is given by

$$\mathbf{q}^*\cdot\boldsymbol{\tau} = -\frac{\partial\phi}{\partial t} \tag{15}$$

where $\boldsymbol{\tau}$ is the tangent to the solid surface. In the far field, the flow is irrotational (except at the wake boundary) and $\mathbf{q}^*$ (and the gradient of its components) should vanish. The components of $\mathbf{q}^*$ are obtained from Equation (11) together with the conditions (14) and (15).

Notice also, that with condition (13) there is one-to-one relationship between the pressure and the potential function according to Equation (12), i.e. given P, one can find ϕ and *vice versa*.

Copyright © 2003 John Wiley & Sons, Ltd.

The $\mathbf{q}^*$ vector should vanish in the inviscid flow region and therefore the solution of the momentum equation can be limited to the viscous region.

Also, the standard Poisson equation for the pressure, obtained by taking the divergence of the momentum equation, is not required and Equation (12) should give the same result (up to truncation errors).

Finally, Equation (10) is not in conservation form. One can update $\mathbf{q}^*$ based on the conservation of the momentum equation via a deferred correction procedure, namely,

$$\mathbf{q} \cdot \nabla \boldsymbol{\delta q}^* + (\boldsymbol{\delta q}^* \cdot \nabla)\nabla\phi - \frac{1}{Re}\nabla^2 \boldsymbol{\delta q}^* = -R_M \tag{16}$$

where $\boldsymbol{\delta q}^*$ is the correction of $\mathbf{q}^*$ and R_M is the momentum equation in conservation form (notice that the viscous stresses in R_M will require the evaluation of third derivatives of ϕ).

2.4. Numerical methods

The present formulation consists of a Poisson equation for the potential function and convection/diffusion equations for the rotational components of the velocity. One can solve all the equations, simultaneously coupled, using Newton's method and a direct solver for the unknowns at each Newton's iteration. This approach is not feasible for general three-dimensional calculations. A segregated approach is used instead, where the potential equation is solved assuming the rotational components of the velocity are known and the momentum equation is used to update the rotational velocities assuming the potential is known. In this case, artificial time-dependent terms are added to the momentum equation to guarantee the convergence of the iterative procedure. Standard numerical methods are employed for all the simple problems treated in this study.

First the domain of interest is discretized using Cartesian grids. This is possible for the simple geometries of the examples considered here. Second, the equations are discretized using finite differences. For the potential equation, central differences are used everywhere. Hence, at a grid point, (i, j), in two dimensions, the discrete equation reads

$$\begin{aligned} &\frac{\phi_{i+1,j} - 2\phi_{i,j} + \phi_{i-1,j}}{\Delta x^2} + \frac{\phi_{i,j+1} - 2\phi_{i,j} + \phi_{i,j-1}}{\Delta y^2} \\ &\quad = -\frac{\bar{u}_{i+1,j} - \bar{u}_{i-1,j}}{2\Delta x} - \frac{\bar{v}_{i,j+1} - \bar{v}_{i,j-1}}{2\Delta y} \end{aligned} \tag{17}$$

where $\bar{u}$ and $\bar{v}$ are the rotational components of the velocity. At a solid surface, the Neumann boundary condition, $\partial\phi/\partial n = 0$, is imposed implicitly, at the discrete level. For example, if the solid surface is horizontal and is placed between grids then the discrete equations at the points next to the surface are modified accordingly. At the point (i, j), Equation (17) becomes

$$\frac{\phi_{i+1,j} - 2\phi_{i,j} + \phi_{i-1,j}}{\Delta x^2} + \frac{\phi_{i,j+1} - \phi_{i,j}}{\Delta y^2} = -\frac{\bar{u}_{i+1,j} - \bar{u}_{i-1,j}}{2\Delta x} - \frac{\bar{v}_{i,j+1} + \bar{v}_{i,j}}{2\Delta y} \tag{18}$$

In Equation (18), we used the relation $(\bar{v}_{i,j} + \bar{v}_{i,j-1})/2 = 0$ at the solid surface, where the point $(i, j-1)$ is fictitious.

Copyright © 2003 John Wiley & Sons, Ltd.

Alternately, if the solid surface is placed at the grid line then

$$\frac{\phi_{i+1,j}-2\phi_{i,j}+\phi_{i-1,j}}{\Delta x^2}+\frac{2\phi_{i,j+1}-2\phi_{i,j}}{\Delta y^2}=-\frac{\bar{u}_{i+1,j}-\bar{u}_{i-1,j}}{2\Delta x}-\frac{\bar{v}_{i,j+1}}{\Delta y} \tag{19}$$

Equation (19) is slightly different but consistent with Equation (18). The equations for the unknown $\phi_{i,j}$ are solved by successive line overrelaxation (SLOR) procedure. The discrete equations for $\bar{u}_{i,j}$ and $\bar{v}_{i,j}$ are given by

$$\begin{aligned}&\frac{\bar{u}^*_{i,j}-\bar{u}^n_{i,j}}{\Delta t}+\bar{u}^n_{i,j}\frac{\bar{u}^n_{i+1,j}-\bar{u}^{n+1}_{i-1,j}}{2\Delta x}-\frac{\Delta x}{2}|\bar{u}^n_{i,j}|\frac{\bar{u}^n_{i+1,j}-2\bar{u}^*_{i,j}+\bar{u}^{n+1}_{i-1,j}}{\Delta x^2}\\&+v^n_{i,j}\frac{\bar{u}^*_{i,j+1}-\bar{u}^*_{i,j-1}}{2\Delta y}+\bar{u}^n_{i,j}\frac{\phi^{n+1}_{i+1,j}-2\phi^{n+1}_{i,j}+\phi^{n+1}_{i-1,j}}{\Delta x^2}\\&+\bar{v}^n_{i,j}\frac{\phi^{n+1}_{i+1,j+1}-\phi^{n+1}_{i-1,j+1}-\phi^{n+1}_{i+1,j-1}+\phi^{n+1}_{i-1,j-1}}{4\Delta x\Delta y}\\&=\frac{1}{Re}\left(\frac{\bar{u}^n_{i+1,j}-2\bar{u}^*_{i,j}+\bar{u}^{n+1}_{i-1,j}}{\Delta x^2}+\frac{\bar{u}^*_{i,j+1}-2\bar{u}^*_{i,j}+\bar{u}^*_{i,j-1}}{\Delta y^2}\right)\end{aligned} \tag{20}$$

and

$$\begin{aligned}&\frac{\bar{v}^*_{i,j}-\bar{v}^n_{i,j}}{\Delta t}+\bar{u}^n_{i,j}\frac{\bar{v}^n_{i+1,j}-\bar{v}^{n+1}_{i-1,j}}{2\Delta x}-\frac{\Delta x}{2}|\bar{u}^n_{i,j}|\frac{\bar{v}^n_{i+1,j}-2\bar{v}^*_{i,j}+\bar{v}^{n+1}_{i-1,j}}{\Delta x^2}\\&+v^n_{i,j}\frac{\bar{v}^*_{i,j+1}-\bar{v}^*_{i,j-1}}{2\Delta y}+\bar{v}^n_{i,j}\frac{\phi^{n+1}_{i,j+1}-2\phi^{n+1}_{i,j}+\phi^{n+1}_{i,j-1}}{\Delta y^2}\\&+\bar{u}^n_{i,j}\frac{\phi^{n+1}_{i+1,j+1}-\phi^{n+1}_{i-1,j+1}-\phi^{n+1}_{i+1,j-1}+\phi^{n+1}_{i-1,j-1}}{4\Delta x\Delta y}\\&=\frac{1}{Re}\left(\frac{\bar{v}^n_{i+1,j}-2\bar{v}^*_{i,j}+\bar{v}^{n+1}_{i-1,j}}{\Delta x^2}+\frac{\bar{v}^*_{i,j+1}-2\bar{v}^*_{i,j}+\bar{v}^*_{i,j-1}}{\Delta y^2}\right)\end{aligned} \tag{21}$$

In Equations (20) and (21), upwind difference approximations of the convective terms in the x-direction are implemented and the terms representing the potential contributions are lagged. The superscript denotes the iteration index (n) and the iterative process represents a vertical line relaxation in the y-direction marching with the main flow in the positive x-direction. The time step Δt, in Equations (20) and (21), must be small enough to ensure stability (see, for example, Reference [4]). Similarly, an upwind difference approximation in the y-direction can be implemented. Also, a horizontal line relation in the x-direction can be used if necessary.

A relaxation parameter β can be introduced in updating $\bar{u}_{i,j}$ and $\bar{v}_{i,j}$, namely,

$$\bar{u}^{n+1}_{i,j}=\bar{u}^n_{i,j}+\beta(\bar{u}^*_{i,j}-\bar{u}^n_{i,j}) \tag{22}$$

$$\bar{v}^{n+1}_{i,j}=\bar{v}^n_{i,j}+\beta(\bar{v}^*_{i,j}-\bar{v}^n_{i,j}) \tag{23}$$

Copyright © 2003 John Wiley & Sons, Ltd.

The boundary conditions at a solid surface are

$$\bar{v}_{i,j} = 0 \tag{24}$$

and,

$$\bar{u}_{i,j} = -\frac{\phi_{i+1,j} - \phi_{i-1,j}}{2\Delta x} \tag{25}$$

If the surface is placed between the grid lines, fictitious points are introduced inside the body and the average of the unknowns at the fictitious points and the points above the surface are used in imposing the boundary conditions.

In the far field, a potential flow is imposed, for example,

$$\phi_x = \text{given} \tag{26}$$
$$\bar{u} = 0 \tag{27}$$
$$\bar{v}_x = \bar{u}_y \tag{28}$$

Other choices are also possible. For example,

$$\bar{u}_y = 0 \tag{29}$$
$$\bar{v}_x = 0 \tag{30}$$

Finally, a two-level strategy can be adopted to improve convergence as follows. First, the viscous flow region is identified and the equation for ϕ, $\bar{u}$, and $\bar{v}$ are solved on a fine mesh with no slip and no penetration boundary conditions at solid surfaces assuming a uniform flow at the outer boundaries. The second step (or level) of calculations is to solve the potential flow equation, with the forcing function, evaluated in the viscous flow region, over the whole domain including the inviscid and viscous flow regions.

This second step provides a better boundary condition at the interface between the viscous and inviscid flow regions. The viscous flow equations are then solved with the new boundary conditions at the interface between the two regions. The process is repeated until convergence. In the second step, an inviscid mesh can be used everywhere provided that the forcing term in the potential equation is integrated over the fine mesh.

3. NUMERICAL RESULTS

Six two-dimensional and four three-dimensional problems were solved numerically in the present work. All two-dimensional problems are solved with both the present potential function method and the standard stream function/vorticity method. The two sets of solutions are in good agreement. For more details see Reference [34].

All computations are done for Cartesian grids using finite-difference method on uniform meshes. Successive line over-relaxation is used as a solver for all tasks. Relaxation parameter is chosen each time for each particular task to achieve faster convergence. Convergence is considered acceptable if the residuals are, at least, 10^{-8}.

Copyright © 2003 John Wiley & Sons, Ltd.

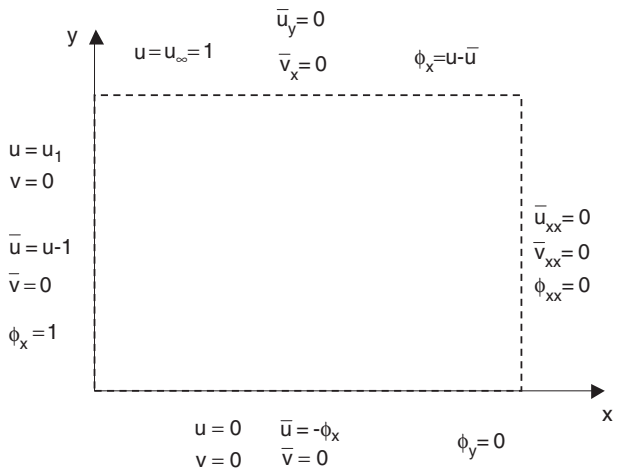

Figure 1. Boundary conditions for an infinite flat plate.

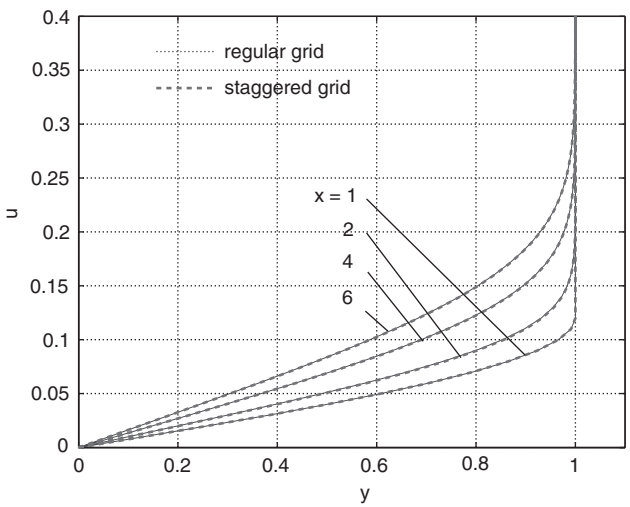

Figure 2. Flow past an infinite flat plate. Profiles of u-velocity obtained using regular and staggered grids.

3.1. *Two-dimensional problems*

Flow past a infinite flat plate: The flow past an infinite flat plate is solved for a domain of (5×0.4) of 41×41 points. The flow at the inlet is a developed boundary-layer flow at $x = 1$, where the boundary layer thickness is $\delta \simeq 5.5/\sqrt{Re}$. Boundary conditions for the present method are shown in Figure 1.

Moreover, the flow past an infinite flat plate was solved over both regular and staggered grids. Both solutions agree with each other (Figure 2).

Copyright © 2003 John Wiley & Sons, Ltd.

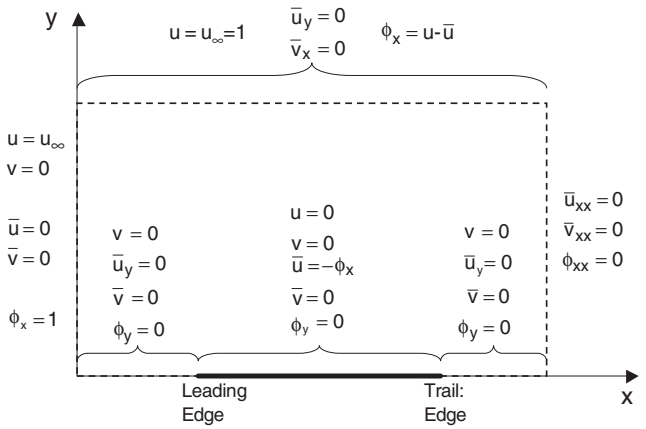

Figure 3. Boundary conditions for finite flat plate.

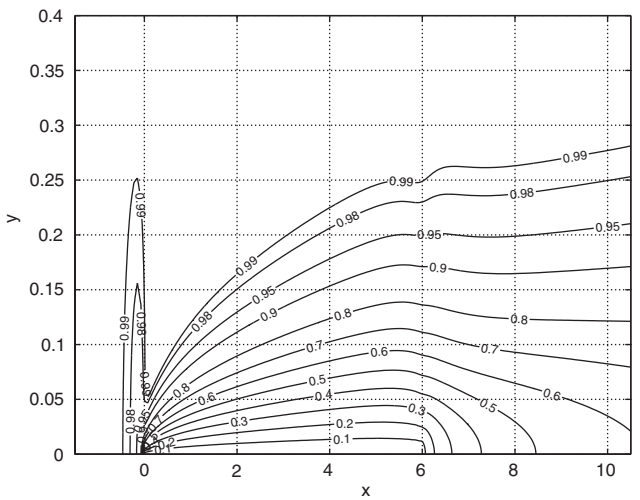

Figure 4. Flow past a finite flat plate. *u*-velocity.

Flow past an finite flat plate: Flow past a finite flat plate is solved for a domain of (10.5×0.4) of 161×161 points. Boundary conditions are shown in Figure 3.

Distributions of the velocities the u and v are shown in Figures 4 and 5 correspondingly. Figures 6 and 7 show the u-velocity and the x-derivative of the potential function at $y = 0$. The development of the u-velocity is shown in Figures 8 and 9. The pressure distribution based on the new modified Bernoulli's law is shown in Figures 10 and 11.

Flow with a pressure jump over a flat plate: The flow with a pressure jump over a flat plate is solved for a domain of (5×0.4) of 81×81 points. Boundary conditions are shown in

Copyright © 2003 John Wiley & Sons, Ltd.

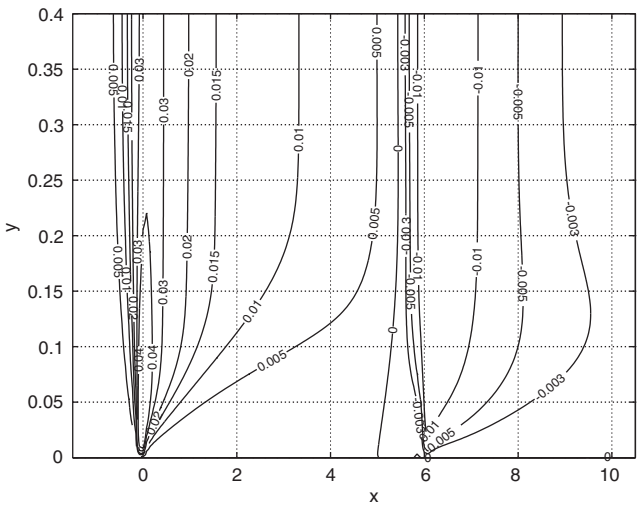

Figure 5. Flow past a finite flat plate. v-velocity.

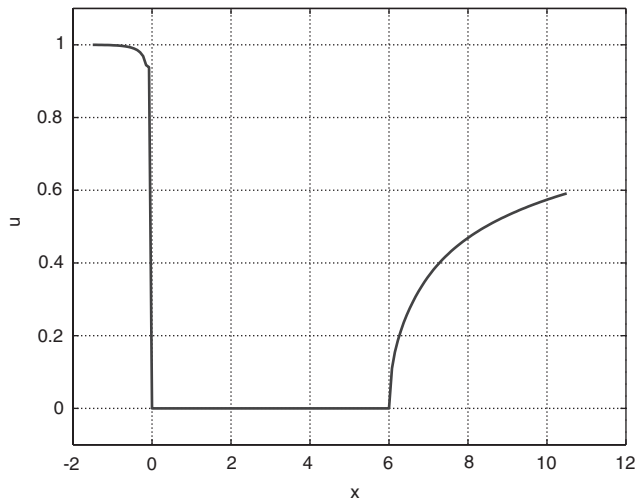

Figure 6. Flow past a finite flat plate. u-velocity at $y = 0$.

Figure 12. The flow at the inlet is a developed boundary layer. The boundary-layer thickness is $\delta \simeq 5.5/\sqrt{Re}$.

A pressure jump is simulated by a jump of the u-velocity at the farfield. For the present case the value of u-velocity changes linearly from 1.0 to 0.87, starting from $x = 2$ until $x = 3$ (see References [14, 42, 43]).

Distributions of the velocities u and v are shown in Figures 13 and 14, respectively.

Flow between two flat plates: Boundary conditions for the flow between two flat plates are shown in Figure 15. Distributions of the velocities u and v are shown in Figures 17 and

Copyright © 2003 John Wiley & Sons, Ltd.

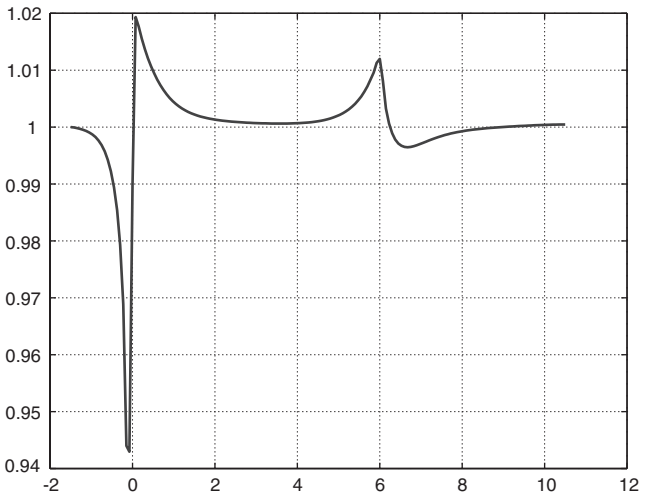

Figure 7. Flow past a finite flat plate. ϕ_x at $y = 0$.

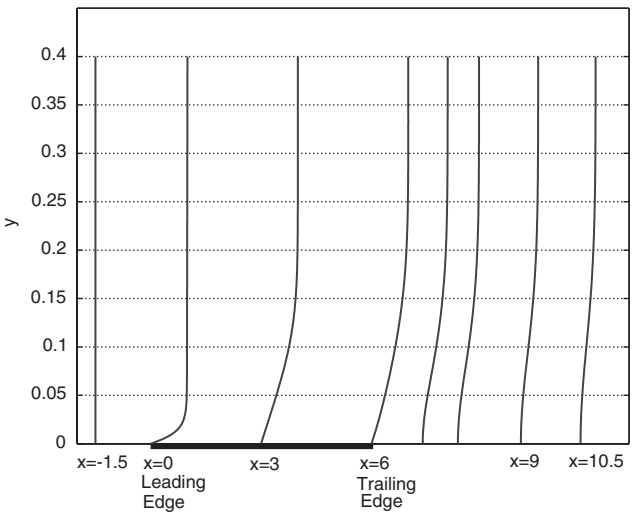

Figure 8. Flow past a finite flat plate. Development of u-velocity.

18, respectively. A domain is 200×1 with 91 points in the x direction (10 points before the plates) and 41 points in the y direction.

Based on dimensional analysis, the entrance length L_e depends on the Reynolds number only:

$$\frac{L_e}{d} = f(Re_d)$$

Copyright © 2003 John Wiley & Sons, Ltd.

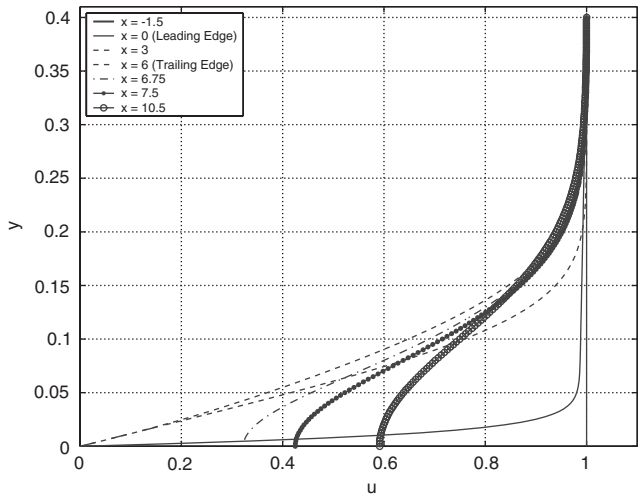

Figure 9. Flow past a finite flat plate. Profiles of u-velocity.

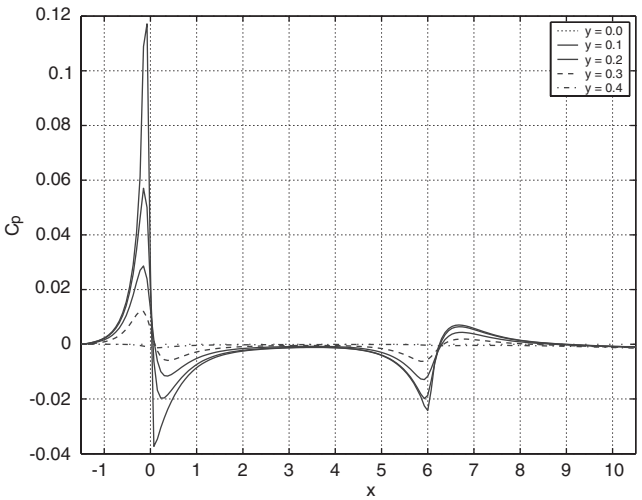

Figure 10. C_p at constant y.

where d is the distance between two plates (see Reference [35]). Figure 16 shows their linear dependence

$$\frac{L_e}{d} = kRe_d \tag{31}$$

where $k \simeq 0.084$.

Copyright © 2003 John Wiley & Sons, Ltd.

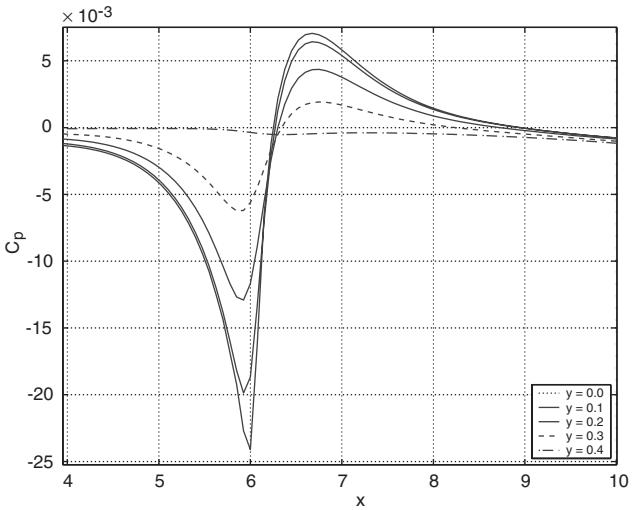

Figure 11. C_p near trailing edge.

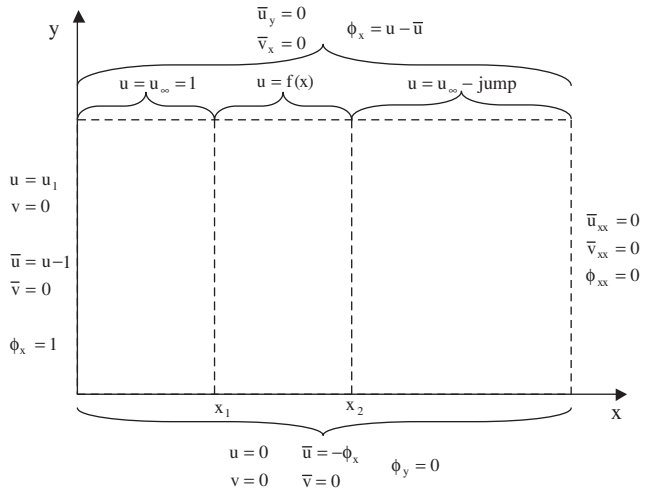

Figure 12. Boundary conditions for the flow with a pressure jump over a flat plate.

Alternately, the boundary-layer thickness for a flow past a flat plate without a pressure gradient at $L = L_e$ is

$$\delta \simeq \frac{5.5}{Re_L} L$$

or,

$$\frac{d}{L} \simeq \frac{11}{\sqrt{Re_L}} = \frac{11}{\sqrt{\rho u d/\mu L/d}} = \frac{11}{\sqrt{Re_d}\sqrt{L/d}}$$

Copyright © 2003 John Wiley & Sons, Ltd.

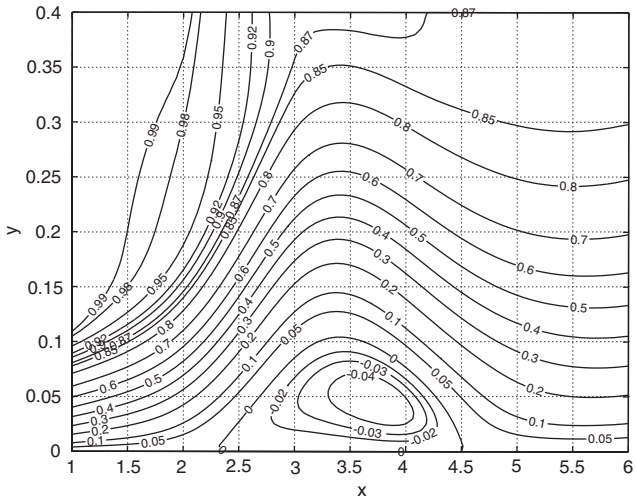

Figure 13. Flow with a pressure jump over a flat plate. *u*-velocity.

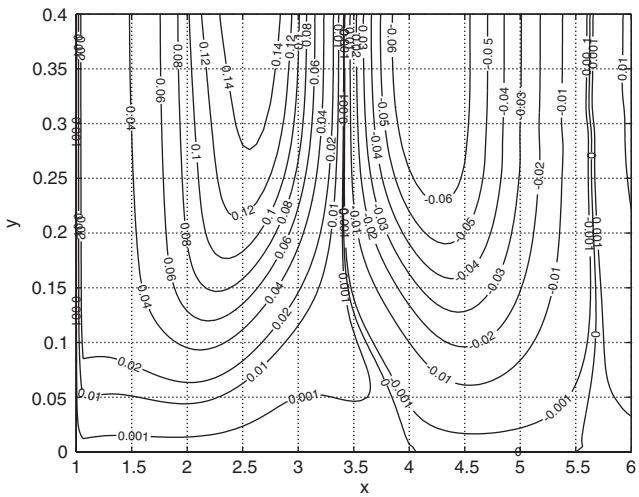

Figure 14. Flow with a pressure jump over a flat plate. *v*-velocity.

Therefore,

$$\frac{L}{d} \simeq 0.0083 Re_d \tag{32}$$

The coefficient k in Equation (31) for the flow between two plates is about 10 times greater than the corresponding coefficient for the flow without a pressure gradient.

Copyright © 2003 John Wiley & Sons, Ltd.

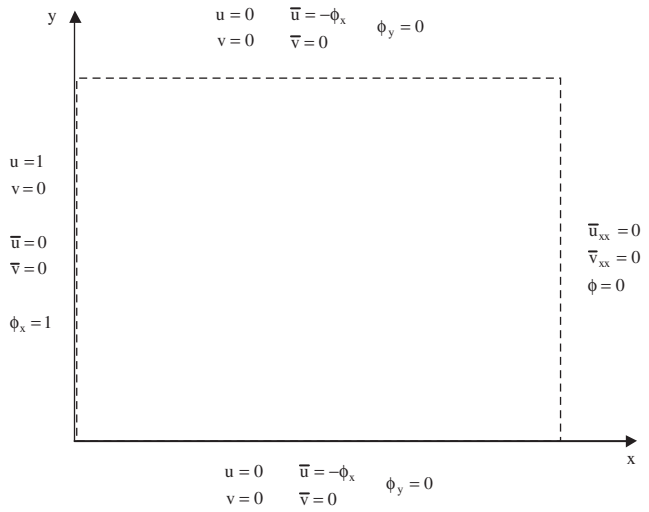

Figure 15. Boundary conditions for the flow between two flat plates.

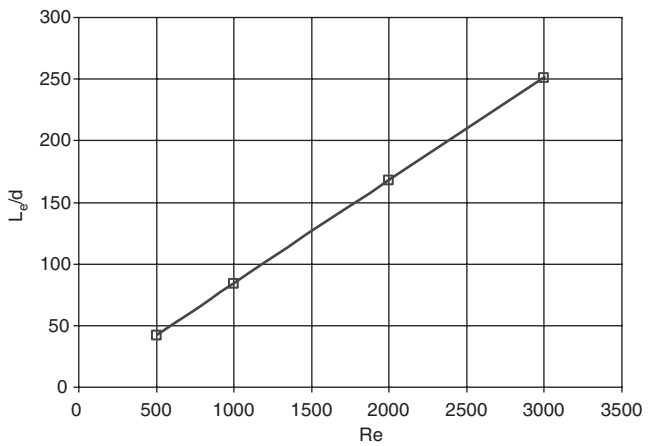

Figure 16. Non-dimensional entrance length vs. Reynolds number.

Flow with suction in a channel between two plates: A flow with suction in a channel between two plates is solved for a domain of (10×0.4) with 81 points in the x direction and 81 points in the y direction. Boundary conditions are shown in Figure 19. The suction is simulated by varying the v-velocity at the upper plate. The value of v-velocity changes as a sine-function (Figure 19) starting from $x = 3$ until $x = 5$, $v_{\max} = 0.15$.

The u and v velocities are shown in Figures 20 and 21.

Flow past an infinite rod: The geometry of a rod and the domain used for the computations are shown in Figure 22. Boundary conditions are shown in Figure 23. The distributions of the velocities u and v are shown in Figures 24 and 25, respectively.

Copyright © 2003 John Wiley & Sons, Ltd.

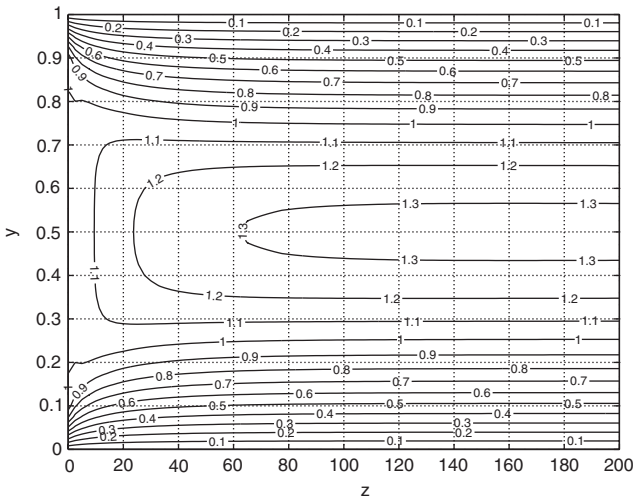

Figure 17. Flow between two flat plates, *u*-velocity.

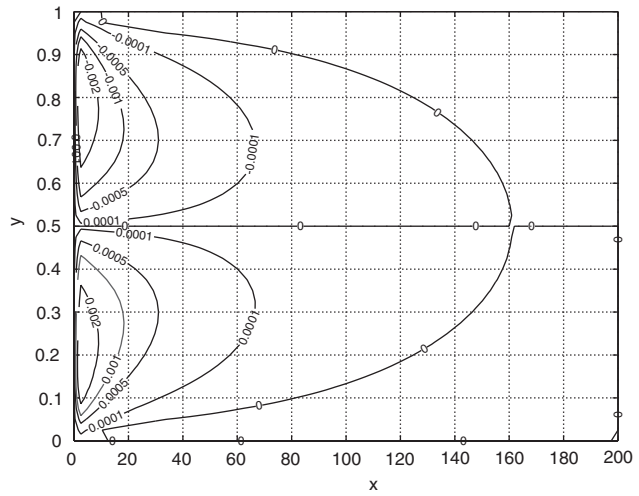

Figure 18. Flow between two flat plates, *v*-velocity.

To avoid problems at the corner of the rod, a staggered grid is used where the solid surface is placed between lines of the grid for the potential function. To study the effect of the corner, more detailed calculations are required.

3.2. Three-dimensional problems

Flow past an infinite swept wing: Computations are done for a flow with $Re = 2080$ over a 45° swept wing. Boundary conditions used for the present computations are shown in

Copyright © 2003 John Wiley & Sons, Ltd.

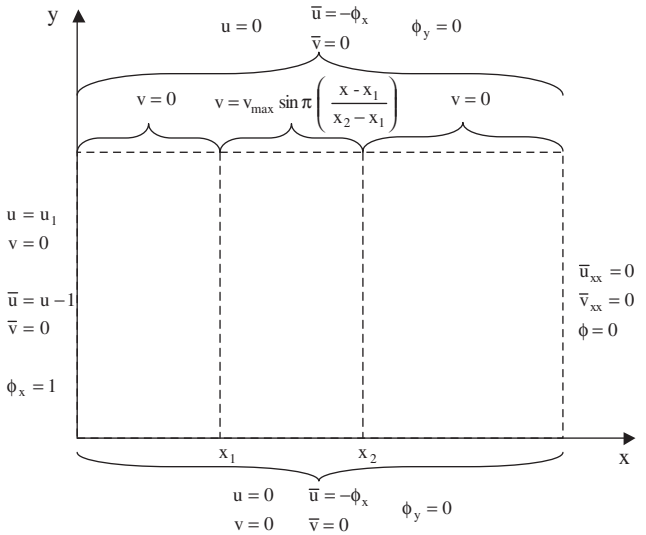

Figure 19. Boundary conditions for flow with suction.

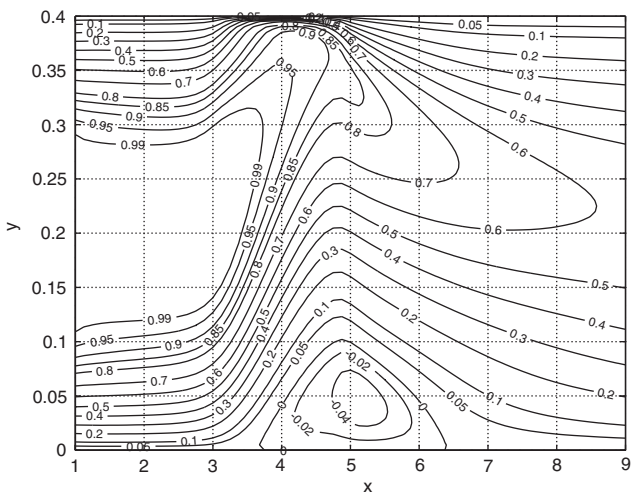

Figure 20. Flow with suction, *u*-velocity.

Figure 26. Figures 27 and 28 show the velocity distributions on the plane of the wing. The calculations are consistent with the law of independence for laminar flows with a constant viscosity [36].

Flow along a corner: A flow along a corner was studied by Carrier [37], Rubin [38], and Stewartson and Howarth [39]. Boundary conditions used for the present computations of a flow along a corner are shown in Figures 29 and 30. The flow far from the corner is assumed

Copyright © 2003 John Wiley & Sons, Ltd.

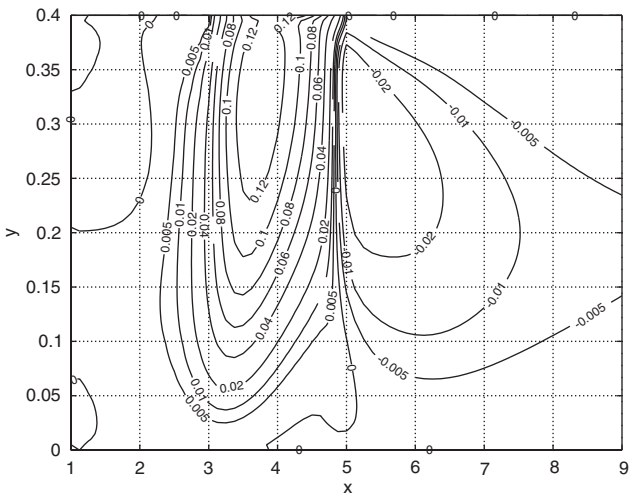

Figure 21. Flow with suction, v-velocity.

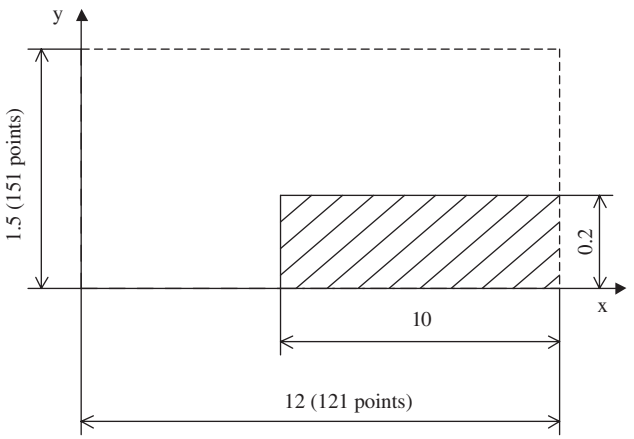

Figure 22. Geometry of a rod.

to be two dimensional. Therefore, boundary conditions for the potential function ϕ at farfield are set as values of ϕ calculated from a 2D flow past a flat plate.

Figure 31 shows a comparison of the u-velocity calculated using the present method with the u-velocity calculated by Carrier in [37]. The present calculations are in good agreement with the results of [37].

Figure 31 is given in the co-ordinates $\eta - \zeta$, where

$$\eta = \frac{y}{\sqrt{vx/u_\infty}}, \quad \zeta = \frac{z}{\sqrt{vx/u_\infty}} \tag{33}$$

Copyright © 2003 John Wiley & Sons, Ltd.

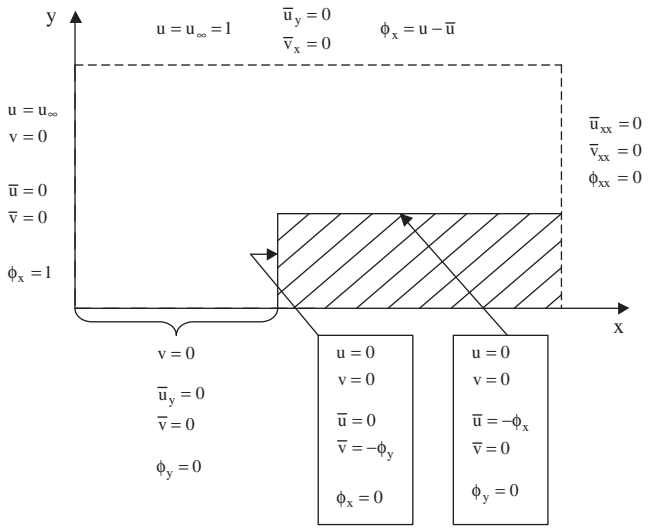

Figure 23. Boundary conditions for the flow past an infinite rod.

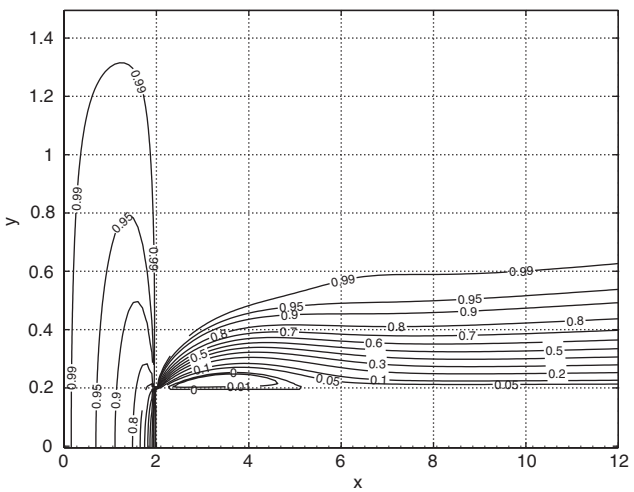

Figure 24. Flow past an infinite rod, *u*-velocity.

Flow in a duct with a square cross-section: Boundary conditions at the inlet and on the solid surfaces of a duct are similar to that of Figure 30. The exit boundary condition for ϕ is $\phi = \text{const}$.

The duct is of length $x = 4$ with a square cross-section $y = z = 0.1$. The velocities in longitudinal $(x - z)$ cross-section are shown in Figures 32 and 33. The velocity distributions in the $y - z$ cross-section (at $x = 0.5$) are shown in Figures 34 and 35. Figure 36 shows *u*-velocity distributions within the fully developed flow region.

Copyright © 2003 John Wiley & Sons, Ltd.

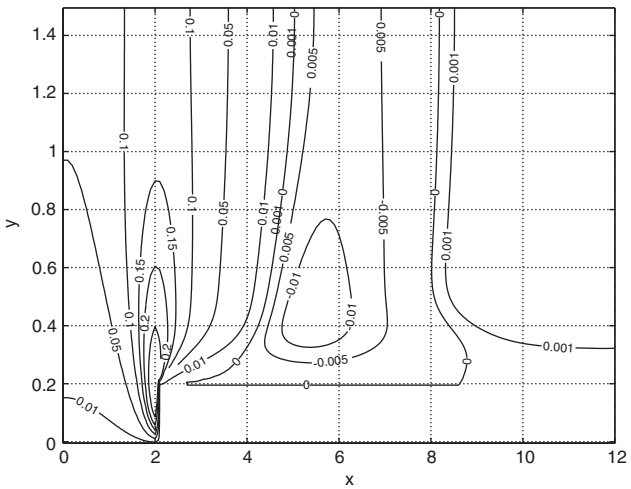

Figure 25. Flow past an infinite rod, *v*-velocity.

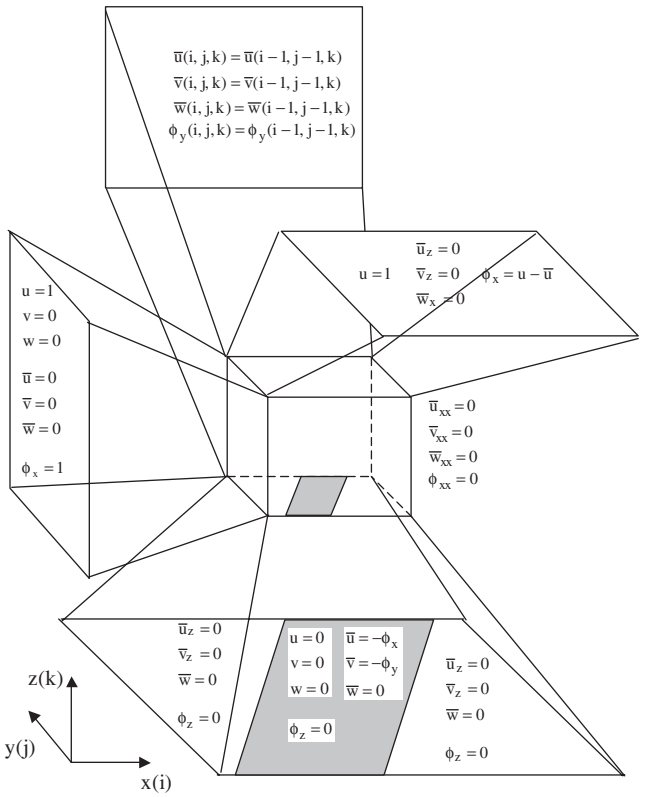

Figure 26. Boundary conditions for the flow past an infinite swept wing.

Copyright © 2003 John Wiley & Sons, Ltd.

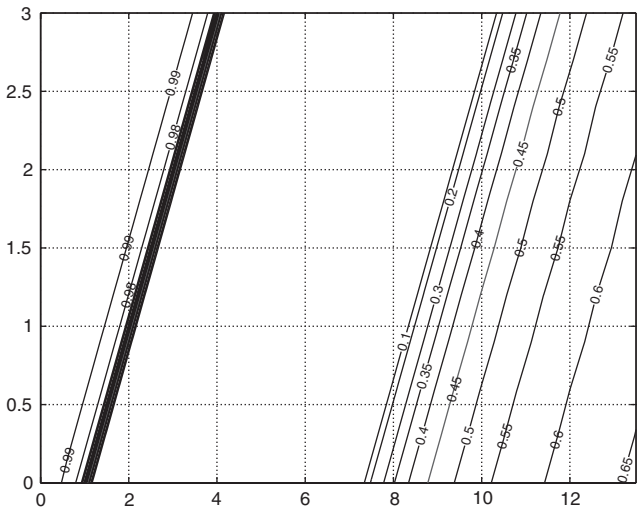

Figure 27. Flow past an infinite swept wing, u-velocity on the plane of the wing.

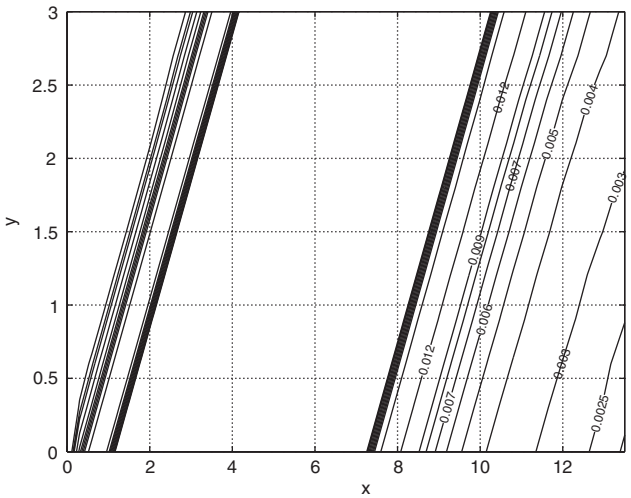

Figure 28. Flow past an infinite swept wing, v-velocity on the plane of the wing.

The relation between the Reynolds number and the nondimensional entrance length is shown in Figure 37.

Dimensional analysis shows

$$\frac{L_e}{d} = kf(Re_d) \tag{34}$$

Copyright © 2003 John Wiley & Sons, Ltd.

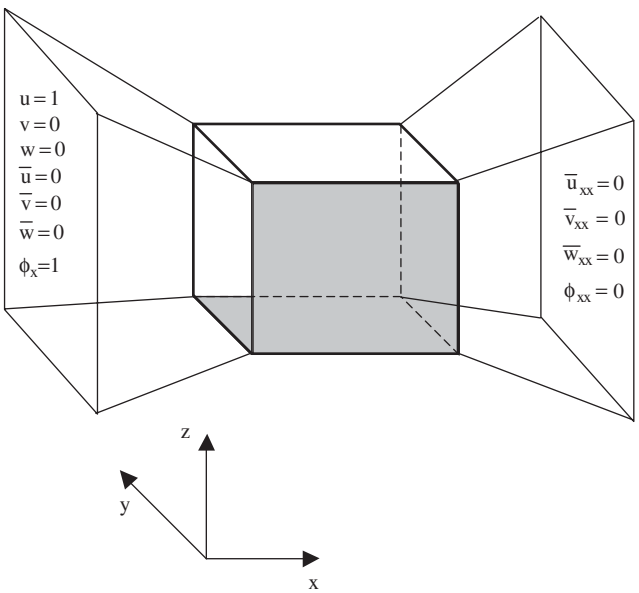

Figure 29. Boundary conditions at the entrance and the exit for the flow along a corner.

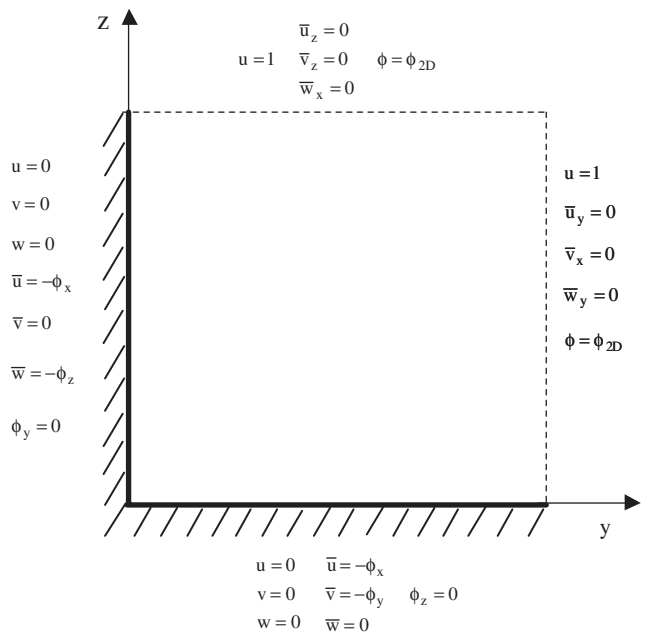

Figure 30. Boundary conditions on side planes for the flow along a corner.

Copyright © 2003 John Wiley & Sons, Ltd.

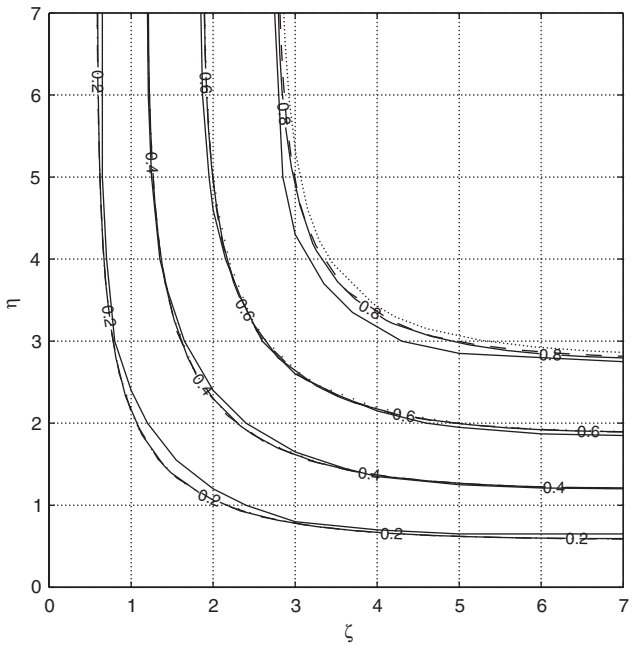

Figure 31. Comparison of *u*-velocity calculated using the present method with *u*-velocity calculated by Carrier (thin lines—present method; thick lines—Carrier).

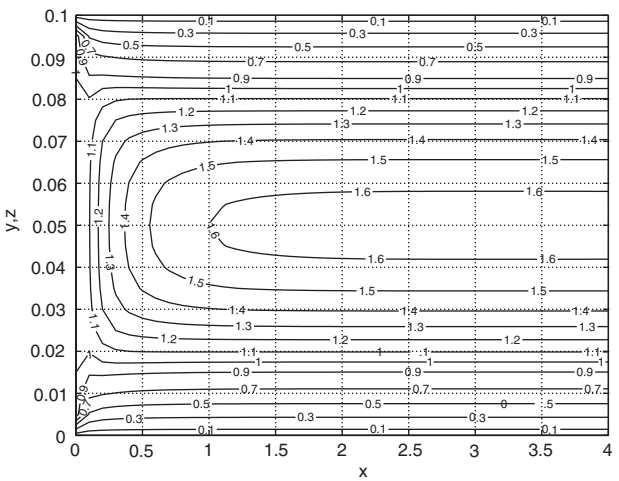

Figure 32. Flow in a duct with a square cross-section, *u*-velocity.

where d is the length of the side of the square cross-section. The present computations show that for a flow in a duct with a square cross-section

$$\frac{L_e}{d} \simeq 0.016 Re_d \tag{35}$$

Copyright © 2003 John Wiley & Sons, Ltd.

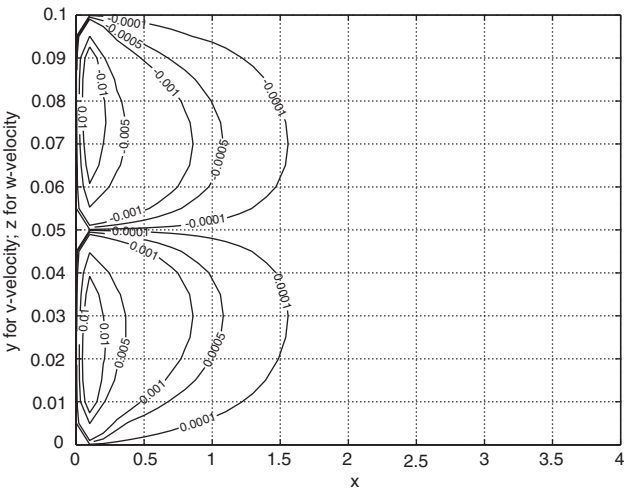

Figure 33. Flow in a duct with a square cross-section, v-velocity ($x - y$ cross-section) and w-velocity ($x - z$ cross-section).

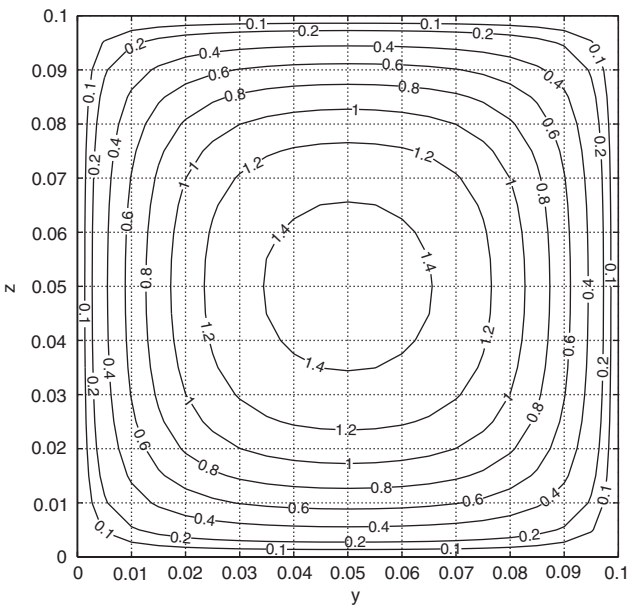

Figure 34. Flow in a duct with a square cross-section, u-velocity in $y - z$ cross-section within entrance length (at $x = 0.5$).

Notice for the two-dimensional case, $k = 0.084$, which is large compared to the three-dimensional case, as expected.

From the momentum equation, for a fully developed flow:

$$u_{yy} + u_{zz} = C = \text{const} \tag{36}$$

Copyright © 2003 John Wiley & Sons, Ltd.

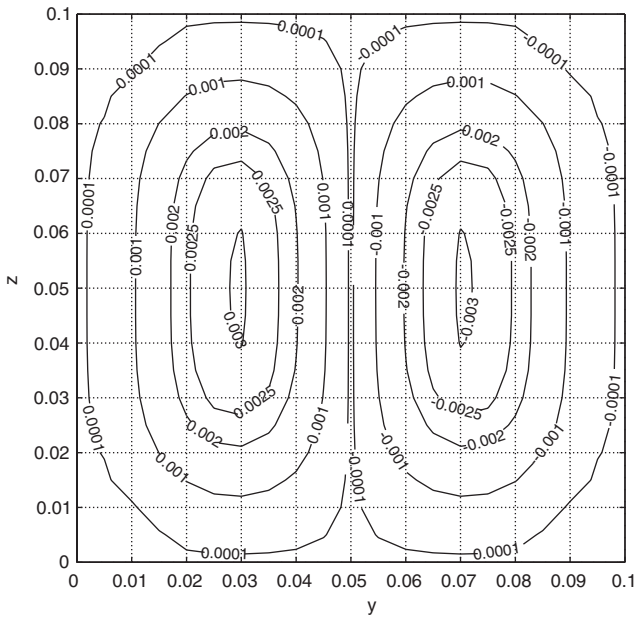

Figure 35. Flow in a duct with a square cross-section, v-velocity in $y-z$ cross-section within entrance length (at $x=0.5$).

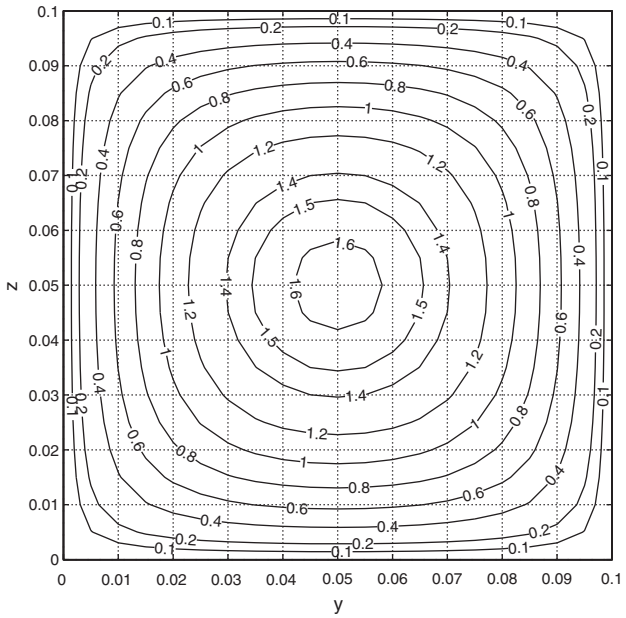

Figure 36. Flow in a duct with a square cross-section. u-velocity in $y-z$ cross-section within fully developed flow region.

Copyright © 2003 John Wiley & Sons, Ltd.

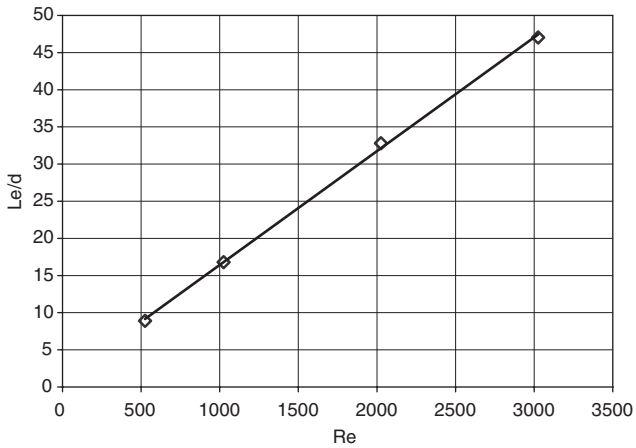

Figure 37. Non-dimensional entrance length vs. Reynolds number for a flow in a duct with a square cross-section.

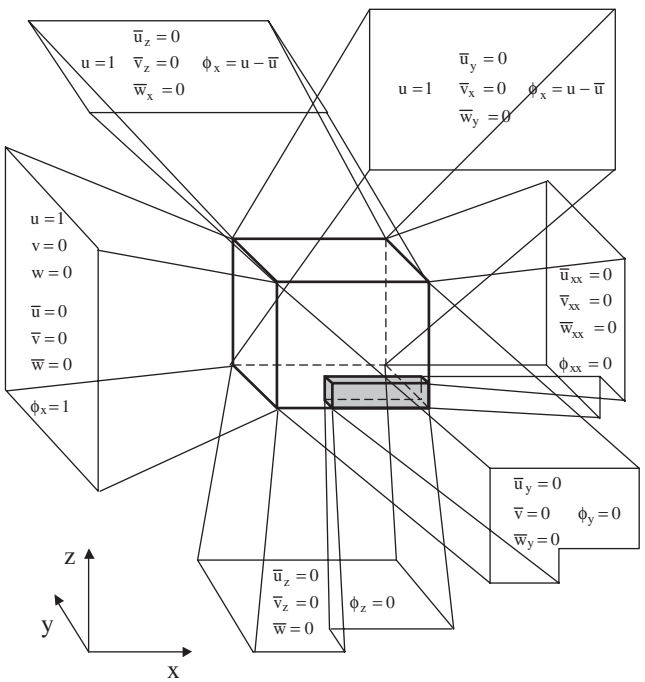

Figure 38. Boundary conditions for a flow over a rod/thin plate on the sides of the domain.

Calculations show for a fully developed flow that the cross-sectional changes of C are less than 1%. Therefore, the computations agree with the fact that C stays constant within a fully developed flow region (see also Reference [40]).

Copyright © 2003 John Wiley & Sons, Ltd.

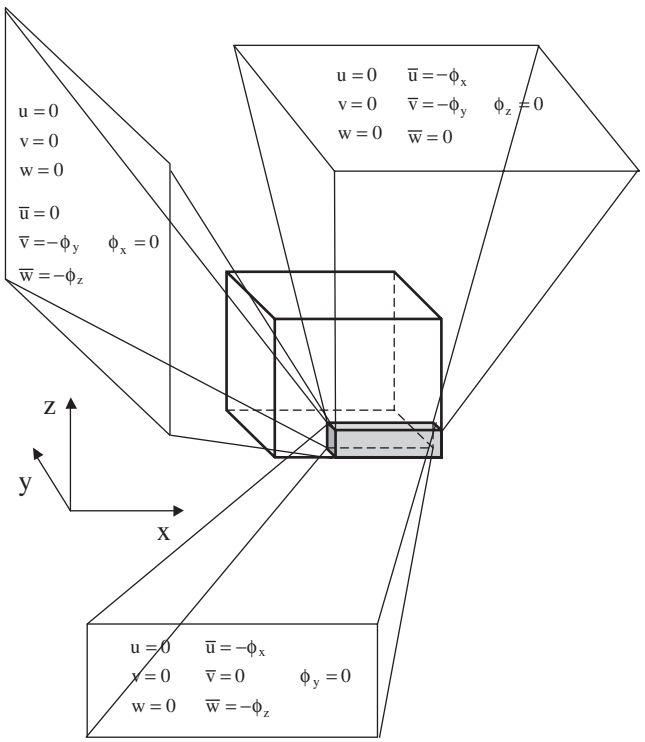

Figure 39. Boundary conditions for a flow over a rod/thin plate on the solid surfaces.

Flow over a rod, and flow over a thin plate: Boundary conditions used in the computations of the flow over a rod are shown in Figures 38 and 39. The number of points in x, y, and z directions is 17, 93 and 93, respectively. The Reynolds number is $Re = 2080$. Figure 40 shows the u-velocity distribution in the $y - z$ cross-section at $x = 3$.

Boundary conditions used in the computations of a flow over a thin plate are the same as for the flow over a rod (Figures 38 and 39). Plate dimensions are 0.15×0.008. Figure 41 shows the u-velocities at a distance $x = 1$ from the leading edge. The number of points in x, y and z directions is 19, 55 and 56, respectively. The Reynolds number is $Re = 1.06 \times 10^5$.

As the edge of the plate is approached, the boundary-layer thickness decreases and the local skin friction rises. Variation of the skin-friction coefficient on a flat plate is shown in Figure 42.

$$C_{\mathrm{f}} = \frac{2}{Re} \frac{\partial u}{\partial z} \tag{37}$$

where, $C_{f\infty}$—skin-friction coefficient far from the side edge of the plate, δ_∞—boundary-layer thickness far from the side edge, and y is the distance from the side edge. This example demonstrates the three-dimensional effect in the neighbourhood of the wing tips. The calculations are consistent with that of Elder [41].

Copyright © 2003 John Wiley & Sons, Ltd.

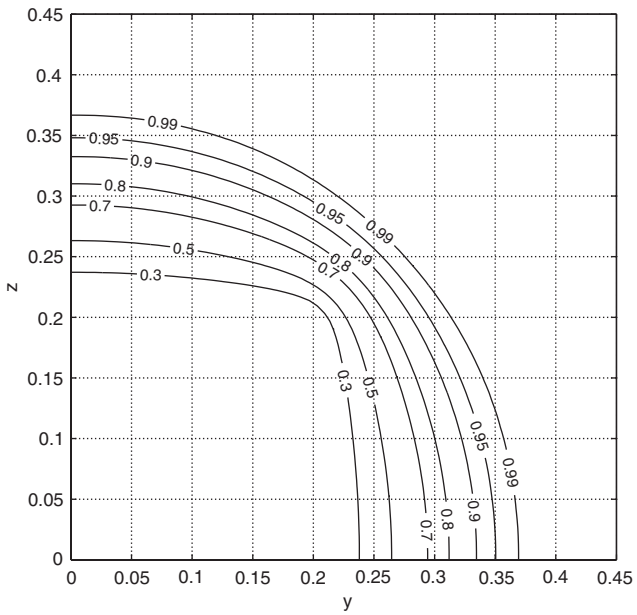

Figure 40. Flow over a rod, u-velocity in $y-z$ cross-section at $x=3$.

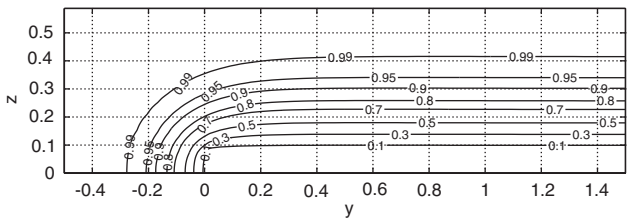

Figure 41. Flow over a thin plate, u-velocity in $y-z$ cross-section at $x=1$.

4. CONCLUDING REMARKS

Numerical simulations of incompressible flows, based on Helmholtz velocity decomposition, are presented. The results confirm the validity of the present formulation for simple two- and three-dimensional problems. Obviously, more sophisticated problems (with complex geometries) can be analysed the same way on either structured or unstructured grids. Standard numerical methods are employed in this work. The formulation is not, however, limited to special discretization or iterative procedures. Accuracy and efficiency can be improved with higher-order schemes and convergence acceleration techniques (e.g. multigrid or GMRES). Further studies are needed to assess the merits of this work quantitatively. For example, how much savings can be achieved with the domain decomposition of inviscid and viscous flows and what would be the gain in accuracy, for a given number of points, due to the fact that no artificial vorticity is generated in the inviscid flow region even with coarse meshes. Finally, the

Copyright © 2003 John Wiley & Sons, Ltd.

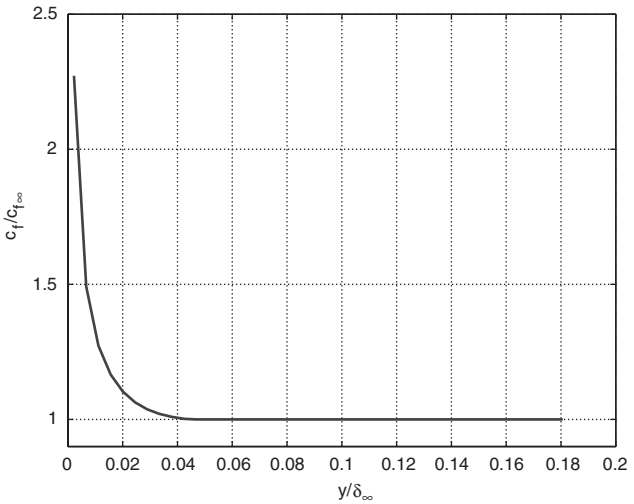

Figure 42. Variation of the skin friction on a flat plate.

present formulation can be extended to time-dependent problems in a straightforward manner using dual-time steps.

REFERENCES

1. Roache PJ. *Computational Fluid Dynamics*. Hermosa Publisher: 1972.
2. Peyret R, Taylor TD. *Computational Methods for Fluid Flow*. Springer: Berlin, 1983.
3. Fletcher CAJ. *Computational Techniques for Fluid Dynamics*, vol. I & II. Springer: Berlin, 1988.
4. Hirsch C. *Numerical Computation of Internal and External Flows*, vols. I, II. Wiley: New York, c1988–c1990.
5. Glowinski R. *Handbook of Numerical Analysis*. Vol. IX. North-Holland: Amsterdam, 2003.
6. Gresho PM, Sani R. *Incompressible Flow and the Finite Element Method*. Wiley: New York, 2000.
7. Zienkiewicz OC, Taylor R. *The Finate Element Method*, vols. I & II. McGraw-Hill: New York, 1989.
8. Harlow FH, Welsh JE. Numerical calculation of time dependent viscous incompressible flow of fluids with free surface. *Physics of Fluids* 1965; **8**:2182–2189.
9. Chorin AJ. A numerical method for solving incompressible viscous flow problems. *Journal of Computational Physics* 1967; **2**:12–26.
10. Kwak D, Kiris C, Dacles-Mariani J, Rogers S, Yoon S. *Computational Fluid Dynamics Review 1998*. World Scientific: Singapore, 1998.
11. Merkle CL, Athavale M. Time-accurate unsteady incompressible flow algorithm based on artificial compressibility. *AIAA Paper 87-1137-CP*.
12. Chorin AJ. Numerical solution of Navier–Stokes equations. *Mathematics of Computation* 1968; **23**:34–45.
13. Tannehill JC, Anderson DA, Pletcher RH. *Computational Fluid Mechanics and Heat Transfer* (2nd edn). Taylor & Francis: London, 1997.
14. Briley WR. A numerical study of laminar separation bubbles using the Navier–Stokes equations. *Journal of Fluid Mechanics* 1971; **47**:713.
15. Briley WR. Numerical method for predicting three dimensional steady viscous flow in ducts. *Journal of Computational Physics* 1974; **14**:8–28.
16. Ghia KN, Hankey WL, Hodge JK. Study of incompressible Navier–Stokes equations in primitive variables using implicit numerical technique. *AIAA Journal paper* 77-648.
17. Tezduyar TE, Behr M, Hughes T. *Computational Fluid Dynamics Review*. Wiley: New York, 1995.
18. Zienkiewicz O, Nithiarasu P, Cordina R, Vazquez P, Ortiz P. The characteristics based split procedure: an efficient and accurate algorithm for fluid problems. *International Journal for Numerical Methods in Fluids* 1999; **31**(1):359–392.
19. Quarteroni A, Valli A. *Domain Decomposition Methods for Partial Differential Equations*. Oxford Science Publications: Oxford, 1999.

Copyright © 2003 John Wiley & Sons, Ltd.

20. Tang C, Hafez M. Finite element/finite volume simulations of viscous flows based on zonal Navier–Stokes formulation. Part I. *Advances in Finite Element Analysis in Fluid Dynamics*, FED-vol. 171. ASME: New York, 1993; 53–66.
21. Tang C, Hafez M. Numerical simulation of steady compressible flows using a zonal formulation. Part I: inviscid flows. *Computers and Fluids* 2001; **30**:989–1002.
22. Tang C, Hafez M. Numerical simulation of steady compressible flows using a zonal formulation. Part II: viscous flows. *Computers and Fluids* 2001; **30**:1003–1016.
23. Nikfetrat K, Hafez M. Numerical solution of the incompressible Navier–Stokes equations using Helmholtz velocity decomposition. *Computational Fluid Dynamics Journal* 2001; **9**(3):266–280.
24. Nikfetrat K, Hafez M. Three dimensional viscous incompressible flow simulation using Helmholtz velocity decomposition. *Computational Fluid Dynamics Journal* 2001; **10**(4):439–445.
25. Dodge PR. Numerical method for 2d and 3d viscous flows. *AIAA Journal* 1977; **15**(7):
26. Glowinski R, Pironneau O. On the mixed finite element approximation of the Stokes problem. *Numerische Mathematik* 1979; **33**:397–424.
27. Ghia KN, Sokhey. Laminar incompressible viscous flow in curved duct of regular cross-section. *Journal of Fluids Engineering* 1977; **99**:640–648.
28. Peeters MF, Habashi WG, Nguyen BQ. Finite element solution of the incompressible Navier–Stokes equations by a Helmholz velocity decomposition. *International Journal for Numerical Methods in Fluids* 1991; **13**: 135–144.
29. Khosla PK, Rubin SG. A review of strongly coupled algorithms for viscous flow problems. *Computers and Fluids* 2001; **30**(7–8):927–938.
30. Gresho PM. On the theory of semi implicit projection methods for viscous incompressible flow and its implementation via a finite element method that also introduces a nearly consistent mass matrix. Part I: Theory. *International Journal for Numerical Methods in Fluids* 1990; **11**:587–620.
31. Issa RI. Solution of the implicitly discretized fluid flow equations by operator splitting. *Journal of Computational Physics* 1985; **62**:40–65.
32. Kim J, Moin P. Application of fractional-step method to incompressible Navier–Stokes equations. *Journal of Computational Physics* 1985; **59**:308–323.
33. Lacor C, Hirsch Ch. Rotational flow calculations in 3-dimensional blade passages. *ASME Paper 82-GT-316*.
34. Shatalov A. Numerical solutions of incompressible Navier–Stokes equations using modified Bernoulli's law. *Master's Thesis*. UC Davis, December 2001.
35. White F. *Fluid Mechanics*. McGraw-Hill: New York, 1986.
36. Schlichting H. *Boundary Layer Theory* (7th edn). McGraw Hill: New York, 1977.
37. Carrier GF. The boundary layer in a corner. *Quarterly of Applied Mathematics* 1947; **4**:367–370.
38. Rubin SG. Incompressible flow along a corner. *Journal of Fluid Mechanics* 1965; **26**:97–110.
39. Stewartson K, Howarth L. On the flow past a quarter infinite plate using Oseen's equations. *Journal of Fluid Mechanics* 1959; **7**:1–21.
40. Rubin SG. Laminar flow in rectangular channel. *Computers & Fluids* 1977; **5**:151–173.
41. Elder JW. The flow past a flat plate of finite width. *Journal of Fluid Mechanics* 1960; **9**:133–153.
42. Briley WR, McDonald H. Numerical prediction of incompressible separation bubbles. *Journal of Fluid Mechanics* 1975; **69**:63–656.
43. Rogers S, Kwak D. An upwind differencing scheme for the incompressible Navier–Stokes equations. *Applied Numerical Mathematics* 1991; **8**:43–64.

Copyright © 2003 John Wiley & Sons, Ltd.